Journal of the European Ceramic Society 40 (2020) 36–48

Contents lists available at ScienceDirect

Journal of the European Ceramic Society

journal homepage: www.elsevier.com/locate/jeurceramsoc

Original Article

Investigation on non-uniform strains of a 2.5D woven ceramic matrix composite under in-plane tensile stress

Xuefeng Teng[a], Duoqi Shi[a,*], Zhen Cheng[a], Xin Jing[b], Shuangqi Lyu[c], Xiaoguang Yang[a]

[a] School of Energy and Power Engineering, Beihang University, Beijing 100083, China
[b] School of Power and Energy, Northwestern Polytechnical University, Xi'an, 710072, China
[c] Aviation Engineering Institute, Civil Aviation Flight University of China, Guanghan, 618307, China

ARTICLE INFO

Keywords:
Ceramic matrix composites
Weave architecture
Unit cell
Strain measurement
Digital image correlation

ABSTRACT

In this study, the digital image correlation technique and strain gauges were applied to the in-plane tensile tests of a 2.5D woven ceramic matrix composite for the purpose of characterizing deformation and strain distribution features. The test results indicate a strong influence of the weave architecture on the strain distribution of the material. Mesoscale finite element models were established based on the weave architecture of the material. The experimental and simulation results show that: the strain distributions are periodic and fluctuating; the maximum strain fluctuation on the surface is about 30%, but the deviation of average strain decreases rapidly with the calculated area increase. The strain measurement methods were proposed to obtain the accurate average strain: the size of measurement/calculated area should be twice larger than the unit cell size; much more accurate result could be obtained when the area size is an integer multiple of the unit cell size.

1. Introduction

Fiber-reinforced ceramic matrix composites (CMCs) have been widely used as structural components in aerospace, civil and automobile industry due to their outstanding physical, mechanical and thermal properties. Design and optimization processes become very important due to material anisotropy in fiber-reinforced CMCs, and requiring more complex analysis. These materials provide the design engineer with a relatively large design space because the stiffness and strength of the composites can be adjusted by changing reinforcement morphology, yarn structure and volume fraction to meet the specifications for particular application [1–4].

Recently, 2.5D woven composites have attracted many attentions due to their excellent mechanical properties in both in-plane and out-of-plane directions. Lots of work has been done to predict the properties [5–7], investigate the damage evolution and failure mechanisms [8–10]. The angle-interlock architecture improves the delamination resistance of 2.5D woven composites, but this would exacerbate the stress/strain concentration and non-uniform distribution in the material. An in-depth understanding of the strain distribution is essential to facilitate the development of material and structure with higher load capacity.

Digital image correlation (DIC) has been proved to be a useful tool for studying the strain distribution of composites, due to its ability to measure displacements and strains on the surface of a deforming specimen in a non-contact way, as well as the full-field measurement capability. In Pan's research [11], significant stress concentration phenomenon was observed on the surface of a 2.5D woven composite, and damage often initiates at the local region where strain is relatively large. The complex weave architecture leads to the non-uniform stress and strain distribution of composites under external loads, and results in the different deformation distributions on the surface and interior of the materials [12–15]. The macroscopic strain strongly depends on the materials structure heterogeneity [12]. Because of bending and straightening of wavy tow segments, strain concentrations at tow crossovers lead to the formation of macroscopic cracks [13,14,16]. During the experiment process, the surface strain is widely used since it is convenient to be obtained. The surface strains of woven composites are periodic and fluctuating, which depend on the weave architecture of the material. Therefore, studying the surface /strain distribution characteristics of the material is of great significance to guide obtaining accurate surface strain.

The heterogeneous strain distribution on the surface of composite can be observed via DIC technique during experimental testing, while the internal strains of material are difficult to obtain. Archer [17] proposed a methodology to accurately embed EFPI (Extrinsic Fabry-Perot Interferometer) fiber optic sensors within the resin channels of woven composites to monitor strain during tensile tests on a woven

* Corresponding author.
E-mail address: shdq@buaa.edu.cn (D. Shi).

https://doi.org/10.1016/j.jeurceramsoc.2019.08.030
Received 4 April 2019; Received in revised form 21 July 2019; Accepted 23 August 2019
Available online 26 August 2019

composite. Digital Volume Correlation (DVC) is an innovative approach for measuring displacement and strain field of a volume from image slices acquired via an X-Ray or CT scanner. Some work has been done to investigate mechanical properties, damage and fracture evolution of material with DVC technique [18–20]. For such studies to be successful, it is important to consider the experimental constraints of increasing X-ray absorption with sample dimension and density, which limits the maximum dimensions and increases time to record tomographs. Also, it is necessary that the microstructure contains sufficient 'speckle' that can be discerned at the experiment's resolution [21]. Besides, validated with the strain field measured by the DIC method, mesoscale finite element (FE) modelling of woven composites can be a powerful tool for studying the strain/stress fields inside the material. This method (FE modeling combined with DIC method) has been used to study various composites, including carbon/epoxy woven composite [22], C/SiC woven composite [23,24], eight harness-satin SiC/SiCN composite [13], twill-weave carbon-fiber-reinforced-plastic composite [25], carbon-epoxy triaxial-braided and glass-poly-propylene twill-woven composite [15]. However, the related work mainly focuses on the 2D woven composites, while the study of 2.5D woven composites is limited yet.

The present paper focus on the non-uniform strain/stress distributions induced by weave architecture of a 2.5D woven CMCs. On-axis tensile experiments along the warp and weft directions were conducted, and 2D DIC technique and strain gauges were used to measure surface strain. Mesoscale finite element model of the composite was established based on the precise descriptions of the weave architecture. Local coordinate systems were assigned on each warp yarn node such that the local coordinate system is always parallel to the local fiber axis, which would shed light on the influence of weave architecture on the local strain fields and contribute to understand stress/strain characteristics of the 2.5D woven composite. FE model was assessed by comparisons of the strain fields measured with DIC method. Through the analysis of experimental and FE simulation results, the deformation and strain distribution characteristics of the 2.5D woven composite were investigated. Finally, the methods to obtain accurate average strain were proposed, which would be helpful during the experiment process.

2. Materials and experiments

2.1. Processing of the SiO_{2f}/SiO_2 composite

Continuous SiO_2 fiber (Feilihua Quartz Glass Corp., China) preforms and silica sol were used to fabricate the 2.5D woven SiO_{2f}/SiO_2 composite. The SiO_2 fiber has a density of 2.2 g/cm^3 and a tensile strength of 1.7 GPa, and the diameter is 6 ~ 7 μm. Prior to the manufacture of the composite, the fibers were woven into 2.5D fabric preform with a volume fraction of 41%.

The 2.5D woven composite (SiO_{2f}/SiO_2) were fabricated by sol-gel method, and silica fiber and silica sol were used as the raw materials [26]. First, the silica fiber fabric was placed in a cracking furnace and heat-treated in a nitrogen atmosphere. The heat-treated silica fiber fabric was then placed in silicone gel under vacuum to be fully infiltrated and dried by heating to form a gel. Finally, the material was placed in a muffle furnace, sintered at 800°C, and converted into ceramic. The above infiltration/sintering processes were cycled 4 times to obtain the final SiO_{2f}/SiO_2 composite. The density of the original composite produced by the above method was about 1.7 g/cm^3. The porosity of matrix was 20% ~ 25%, and the specific surface area was up to 1000 m^2/g. The volume fractions of warp and weft yarns are 30.13% and 12.85% respectively.

The tensile specimens of the 2.5D woven SiO_{2f}/SiO_2 composite were cut from a large SiO_{2f}/SiO_2 composite sheet with the warp yarn and weft yarn aligned to the loading direction, respectively. The dimensional size was 10 mm × 100 mm × 2.2 mm (width × length × thickness). The local architecture of the specimen is presented in Fig. 1.

2.2. Experimental setup and procedure

The in-plane tension tests including warp and weft directions were carried out by an electronic universal testing machine INSTRON 5966 with a force range of ± 10kN. The machine has sufficient control precisions of force within 0.5% and displacement within 0.1%. The displacement loading rates of tension tests were 0.6 mm/min.

In order to study the influence of weave architecture on strain distributions and deformation characteristics of the 2.5D woven composite, displacement and strain fields on the specimen surface were measured with the 2D DIC method and strain gauges. Prior to the experiments, one side of the specimen was sprayed with speckle and the other side was attached with a strain gauge. To ensure the strain gauge adheres well to the material, a thin layer of epoxy resin was applied on the surface before the strain gauge was attached with 502 glue. The modulus of epoxy resin (~ 1 GPa) is much lower than those of the fiber and matrix, and the thickness is also much thinner than the specimen. Therefore, the influence of glue on the strain/stress behavior can be ignored. Besides, the strain can be transferred to strain gauge effectively. The imaging system was then placed in front of the specimen with the optical axis of the camera perpendicular to the speckle surface, as shown in Fig. 2.

The images were recorded with industrial telephoto lens with a focal length of 75 mm and a CCD camera with a resolution of 2592 × 1944 pixel, and the recording frequency was 1 Hz. The software used for DIC calculation and analysis of speckle images before and after deformation was Vic-2D 2009(Correlated Solutions, Inc. U.S.A). The subset and step sizes used in the calculation were 29 pixels and 5 pixels.

3. Finite element modeling of the 2.5D woven composite

3.1. Geometrical model

The mechanical properties of woven composites are primarily dependent on the architecture of fiber preform. Therefore, an accurate description of the weave architecture is necessary and essential to obtain the accurate simulation results. The traditional representative volume cell (RVC) of 2.5D woven composites (Fig. 3) was not adopted in this paper. Since the layer of yarn is pretty few and the RVC could repeat only twice in Y direction, and the weave architecture of top and bottom surfaces are quite different with RVC. Therefore, the mechanical behaviors of 2.5D woven composites could not be obtained accurately through the analysis of the RVC, especially for the surface stress/strain distributions. The architecture of the 2.5D woven composite is shown in Fig. 4. It consists of a multi-layer woven warp yarns and a set of straight weft yarns, and adjacent weft yarns are interwoven by warp yarns. Liu [27] proposed a three-unit-cell model which introduced a new type of cell (transitional cell) into traditional method of cell partition in the elastic prediction of 2.5D composites, the three-unit-cell model divided 2.5D composites into surface cell, transitional cell and body cell. The result shows the difference between transitional cell and body cell cannot be ignored, which directly confirm the necessity of the cell-partition method in elastic prediction. Therefore, accurate modeling of the architecture, especially the modeling of surfaces, is essential for investigating the mechanical behavior and strain distributions of 2.5D woven composites.

The specimens were observed with trinocular reflection digital metallurgical microscope (TRDMM) to determine the cross-sectional shape and size of the warp and weft yarns. Due to the deformation of the yarns during the fabrication process, the cross-sectional shapes are

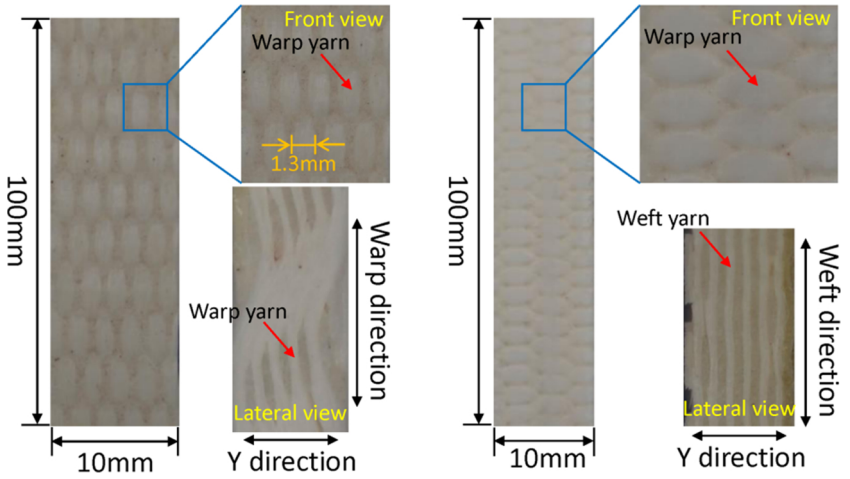

Fig. 1. 2.5D woven SiO_{2f}/SiO_2 composite (warp direction and weft direction).

irregular. But the cross-section of weft yarn is close to an ellipse and warp yarn cross-section close to a racetrack shape. The axis of the weft yarn is assumed to be straight, and the center line of the warp yarn consists of two parts: the arc in the interlocking area and straight line in the rest (as shown in Fig. 5). The FE model was established based on the wearing parameters (Table 1), which were measured with TRDMM. The rest parameters can be calculated as Eq. 1 and Eq. 2.

$$e = d - c \tag{1}$$

$$\varphi = \arctan\left(\frac{L}{R}\right) \tag{2}$$

where *Lx*, *Ly* and *Lz* represent the length, thickness and width of the unit cell, *a* and *b* are the width and thickness of weft yarns, while *d* and *e* are the width and thickness of warp yarns. *R* is the arc radius of warp yarn curve, *L* is the projection length of the curve arc along the X direction. And φ is the dip angle of the straight segment of the warp yarn. With the geometrical parameters determined, the unit cell model can be established precisely.

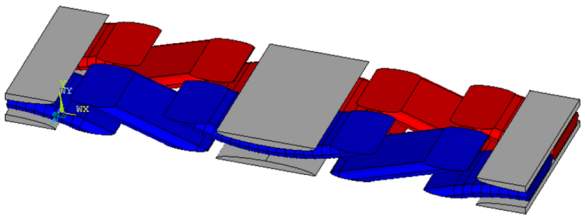

Fig. 3. Traditional representative volume cell of 2.5D woven composites without matrix domains.

3.2. Boundary condition and material properties

3D FE models of the specimen were constructed to study the tension behavior of the 2.5D woven composite, using commercially available software ABAQUS 6.14. The element type were C3D8R (tows) and C3D4 (matrix).

Since the cross section of the specimen contains only a few representative volume units, the periodic boundary conditions are not

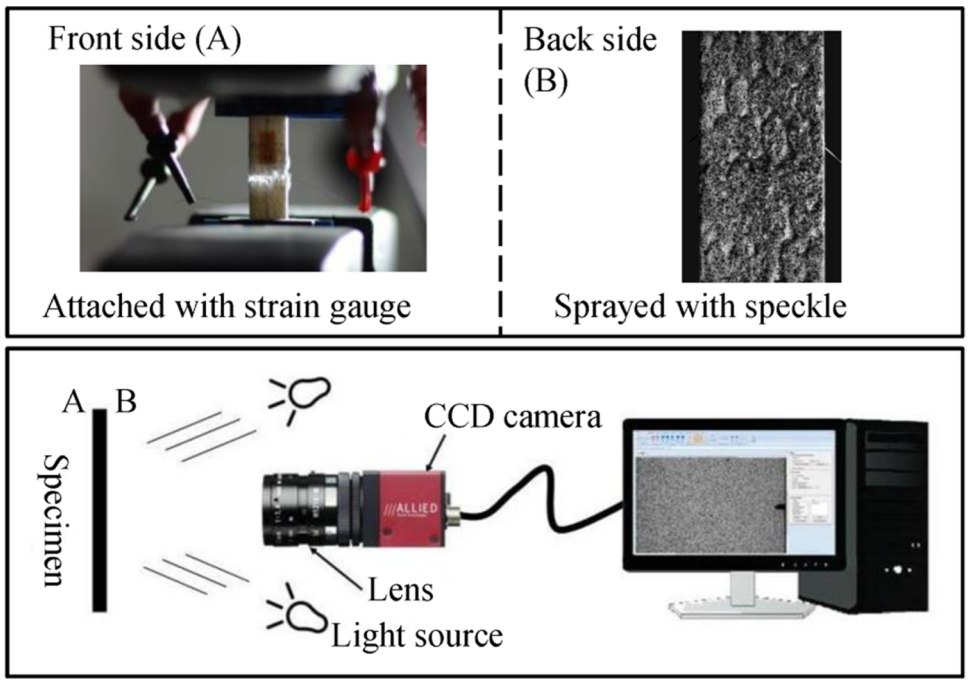

Fig. 2. Experiment schematic and strain measurement methods.

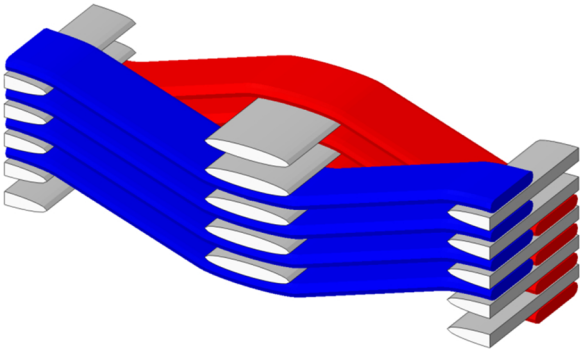

Fig. 4. Weave architecture of 2.5D woven composites without matrix domains.

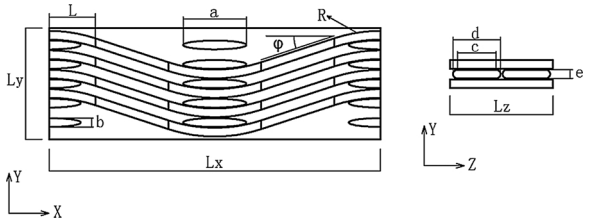

Fig. 5. Illustration of the parameters in the 2.5D woven composite.

Table 1
Weaving parameters in 2.5D woven composite (mm).

Lx	*Ly*	*Lz*	*a*	*b*	*c*	*d*	*R*	*L*
6.82	2.30	2.12	1.3	0.182	0.8	0.98	3.05	0.9527

applicable to the FE model in the Y and Z directions. The established FE models have the same cross sections as the test specimens, see Figs. 1 and 6 (the tow mesh and matrix mesh are shown separately, to illustrate the meshed weave architecture of the tows in the FE model). The periodic boundary conditions are applied in X direction (loading/vertical direction), while free boundary conditions are employed in the Y and Z directions (transverse directions).

The interfaces between the fiber tows and the matrix are not considered and simulated. Therefore, no contact criterion is adopted here; and on the surface of the tows and the matrix, the tow elements and the matrix elements share the same nodes (see Fig. 7).

The micro-RVE (shown in Fig. 8) with periodic boundary conditions was used to back out the elastic properties of fiber yarn at meso-scale. The length and width of the RVE are set as unit value, therefore the height is $\sqrt{3}$. Based on the fiber volume fraction (0.41) which was observed from the fiber yarn cross section with SEM, the fiber diameter is set as 0.672. The elastic properties used in micro-RVE model are listed in Table 2. The predicted values of elastic properties of fiber yarn are listed in Table 3. And the properties of SiO_2 matrix at meso-scale are given in Table 4.

3.3. Local coordinate systems of warp yarn

In fiber-reinforced CMCs, the crimp of the warp yarn causes the local fiber axis to rotate relative to the global coordinate system along the length of the yarn, which results in a change of effective modulus in the global direction. Besides, the warp yarns are transversely isotropic material, it is necessary to assign a local coordinate system to each yarn node so that the local fiber axis is always parallel to the local 1 direction of the yarn length. However, creating local coordinate systems and assigning the local coordinate system to each element in the geometrical model can be complicated. To simplify the modeling process, the global coordinate system is assigned to the warp yarn model, and then is rotated to obtain the local coordinate system at each warp yarn node in ABAQUS user material subroutine.

For a given warp yarn node, there is a rotation of α along the Z axis between the local coordinate system and the global coordinate system, as shown in Fig. 9.

The cosine values of the angles between the global coordinate and local coordinate compose an orthogonal matrix. And the relationship of stress/strain tensor between global and local coordinates could be written as:

$$[\sigma_l] = [A][\sigma_g][A^{-1}] \tag{3}$$

$$[\varepsilon_l] = [A][\varepsilon_g][A^{-1}] \tag{4}$$

$$[A] = \begin{bmatrix} a_{11} & a_{12} & a_{13} \\ a_{21} & a_{22} & a_{32} \\ a_{31} & a_{32} & a_{33} \end{bmatrix} \tag{5}$$

where $[A]$ is the orthogonal matrix, $[\sigma_l]$, $[\varepsilon_l]$, $[\sigma_g]$ and $[\varepsilon_g]$ represent the stress/strain tensor in the local and global coordinates, respectively. a_{ij} (i,j = 1,2,3) is the cosine of the angle between global axis i and local

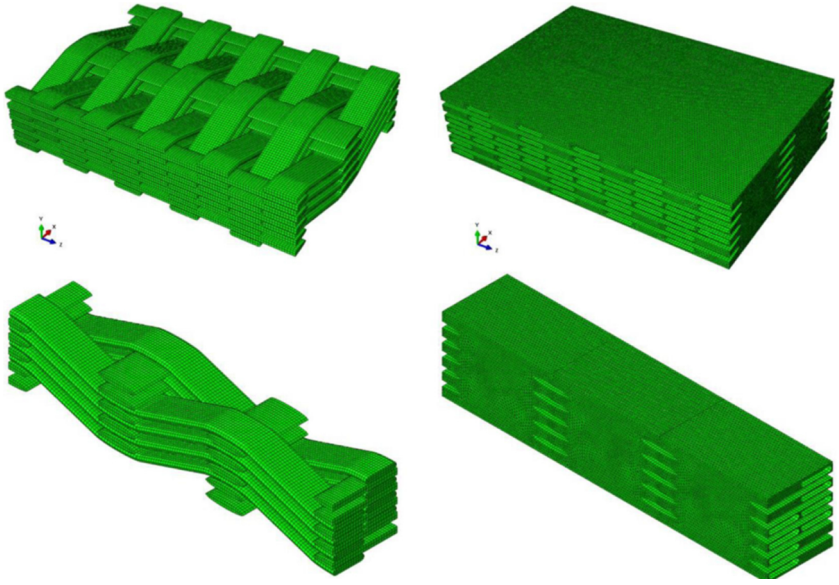

Fig. 6. Meshed model of the FE model at meso-scale.

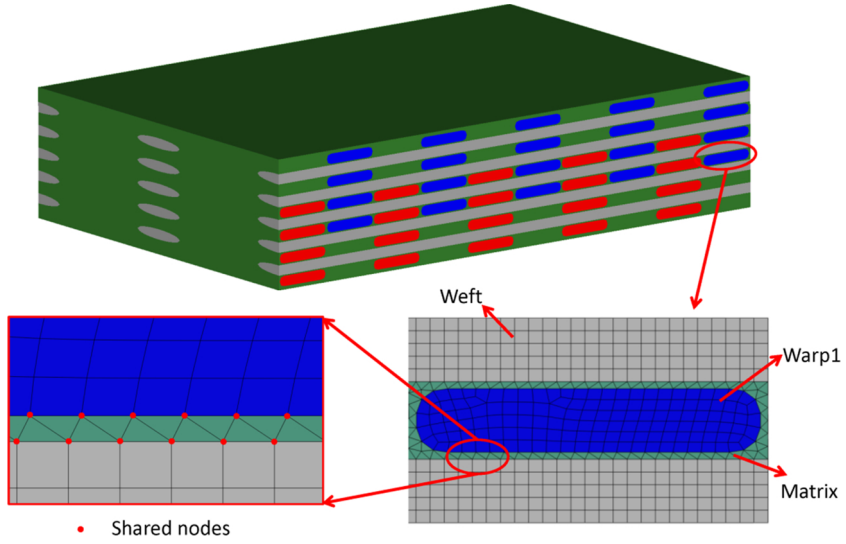

Fig. 7. Shared nodes of the tow elements and the matrix elements on the interface.

axis j, $a_{ij} = cos(x_i^{'}, x_j)$.

Expanding the Eq.3 and Eq.4 into vector form,

$$\sigma_g = [M]\sigma_l \tag{6}$$

$$\varepsilon_g = [M]\varepsilon_l \tag{7}$$

$$[M] = \begin{bmatrix} a_{11}^2 & a_{12}^2 & a_{13}^2 & 2a_{12}a_{13} & 2a_{11}a_{13} & 2a_{11}a_{12} \\ a_{21}^2 & a_{22}^2 & a_{23}^2 & 2a_{22}a_{23} & 2a_{21}a_{23} & 2a_{21}a_{22} \\ a_{31}^2 & a_{32}^2 & a_{33}^2 & 2a_{32}a_{33} & 2a_{31}a_{33} & 2a_{31}a_{32} \\ a_{21}a_{31} & a_{22}a_{32} & a_{23}a_{33} & (a_{22}a_{33}+a_{32}a_{23}) & (a_{23}a_{31}+a_{33}a_{21}) & (a_{21}a_{32}+a_{31}a_{22}) \\ a_{31}a_{11} & a_{32}a_{12} & a_{33}a_{13} & (a_{32}a_{13}+a_{12}a_{33}) & (a_{33}a_{11}+a_{13}a_{31}) & (a_{31}a_{12}+a_{11}a_{32}) \\ a_{11}a_{21} & a_{12}a_{22} & a_{13}a_{23} & (a_{12}a_{23}+a_{22}a_{13}) & (a_{13}a_{21}+a_{23}a_{11}) & (a_{11}a_{22}+a_{21}a_{12}) \end{bmatrix} \tag{8}$$

where $[M]$ is the transformation matrix from the global coordinate system to the local coordinate system. And the global stiffness matrix $[C_g]$ of each node can be calculate with local stiffness matrix $[C_l]$ and transformation matrix $[M]$:

$$[C_g] = [M] \bullet [C_l] \bullet [M]^{-1} \tag{9}$$

For the FE model established in this paper, a global coordinate system was assigned to the model, and the coordinate rotation processes of yarns were conducted in ABAQUS umat. The yarns were divided into three groups: weft yarns (gray parts in Fig. 3), the first (blue

Table 2
Material properties of constituents at micro-scale.

	Young's Modulus	Poisson's ratio
fiber	75GPa [28]	0.25 [28]
matrix	35GPa [29]	0.16 [30]

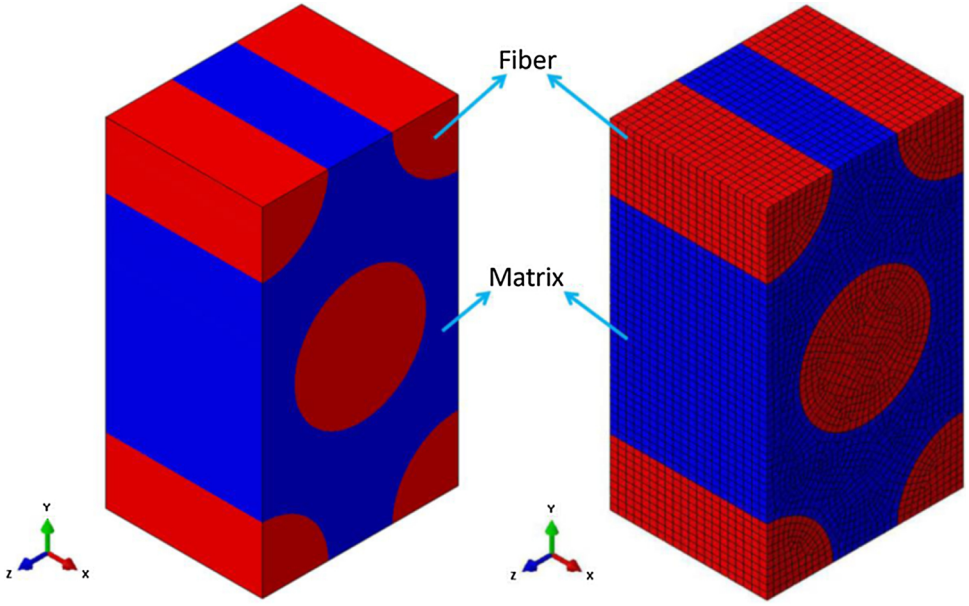

Fig. 8. Geometrical and mesh model of micro-RVE.

Table 3
Predicted properties of fiber yarn.

	Vertical Modulus (GPa)	Transverse Modulus (GPa)	Vertical Shear Modulus(GPa)	Transverse Shear Modulus(GPa)
Fiber yarn	51.36	46.60	18.89	18.53

Table 4
Material properties of SiO_2 matrix at meso-scale.

	Young's Modulus	Poisson's ratio
SiO_2 matrix	6 GPa	0.25

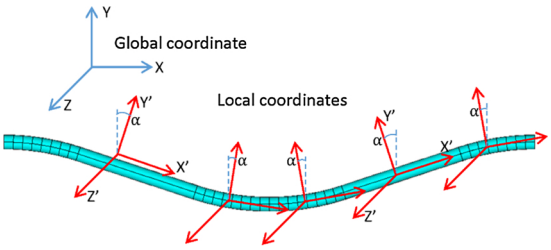

Fig. 9. Crimp of warp yarn and local coordinates.

parts in Fig. 3) and the second (red parts in Fig. 3) set of warp yarns. For the weft yarns, the local coordinate system can be rotated 90 ° along the Y axis from the global coordinate system. For the first and second set of warp yarns, the local coordinate system can be obtained by rotating the global coordinate system along the Z axis, but with opposite direction. Here, the sine and cosine value of the first set of warp yarns are calculated as an example:

$$\sin\alpha = \begin{cases} -X/R & 0 \le X < L \\ -L/RL \le X < \frac{1}{2}L_x - L & \\ \left(X - \frac{1}{2}L_x\right)\Big/R\frac{1}{2}L_x - L \le X < \frac{1}{2}L_x + L & \\ L/R\frac{1}{2}L_x + L \le X < L_x - L & \\ -(X - L_x)/RL_x - L \le X \le L_x & \end{cases}$$

$$\cos\alpha = \sqrt{1 - (\sin\alpha)^2} \quad 0 \le X \le L_x \tag{10}$$

With the sine and cosine of the rotation angle, a_{ij} (i,j = 1,2,3) can be calculated easily. Then the transformation matrix $[M]$ can be obtained.

3.4. Validation of mesh convergence

The quality of the mesh is important for the accuracy of the predicted results. The mesh choice was based on a mesh refinement analysis by comparing the normalized moduli (divided by the effective moduli of the model with an element edge length of 0.02 mm) of the models. Here, the element edge lengths with 0.1 mm, 0.05 mm, 0.04 mm, 0.025 mm, and 0.02 mm are chosen. The local diagrams of the meshed models are shown in Fig. 10 with the change of the element size clearly observed. It can be observed that changes between the normalized moduli for the different meshes are limited (less than 3%, as shown in Fig. 11). The trends and results made with these analyses are not expected to change drastically with further mesh refinements, and there is good agreement between the results. However, with the mesh size decrease, the computing time increases significantly. Considering both the accuracy of simulation result and the cost of computing, the element size is set as 0.04 mm.

4. Results and discussion

4.1. Experimental investigation

4.1.1. Strain distribution

The full-field strain distributions of the specimen surface were extracted with the recorded images during the experiments. Fig. 12 shows the full-field vertical and transverse strain contours under warp direction tensile stress of 20 MPa, 40 MPa, 60 MPa, 80 MPa and 100 MPa, respectively. Fig. 13 shows the full-field vertical and transverse strain contours under weft direction tensile stress of 10 MPa, 20 MPa, 30 MPa, 40 MPa and 50 MPa, respectively. It can be seen from Figs. 12 and 13 that the strain distributions on the surface of the 2.5D woven composite exhibit periodic variability, which are related to the weave architecture of warp and weft yarns.

As shown in Fig. 12(a), the vertical strains on the surface of matrix are larger than the vertical strains on the surface of warp yarns. The warp yarns are curved and have a stretch tendency under warp direction tensile loads. Therefore, the spacing between the weft yarns gets larger. Besides, the modulus of matrix is lower than the modulus of yarns. These result in a larger vertical strain in the matrix.

Due to the larger strain and lower strength of the matrix, micro-cracks initiate and propagate along the matrix on the specimen surface. The matrix cracks also indicate micro-damage of the yarns in the material. The load capacity of damaged yarns decrease and more load is transferred to the adjacent matrix, leading to the stress and strain of the matrix increasing and the initiation of cracks. The micro-cracks initiate in different matrix regions when the applied load reaches about 70% of the tensile strength. Then these cracks propagate and form a main crack, and the brittle fracture of the specimen occurs.

4.1.2. Macroscopic mechanical behavior

Figs. 12 and 13 show the strain evolution process of the 2.5D woven SiO_{2f}/SiO_2 composite under in-plane warp/weft direction tensile loadings, respectively. Micro-cracks on the specimen surface initiated at the stress of 80 MPa (warp direction loading) and at 40 MPa (weft direction loading). With the applied load increase, small cracks propagate and form a main crack. When the stress on the crack cross section reaches the tensile strength, the fiber fracture and pull-out occur. The material exhibits brittle mechanical behavior. No evident surface crack was found at the stress lower than 80% of the strength, and the fiber fracture occurred suddenly at the tensile strength, resulting in the load decrease to zero immediately, as shown in Fig. 14.

The average transverse strains and vertical strains of the 2.5D woven SiO_{2f}/SiO_2 composite are calculated with DIC method. Fig. 15 shows the stress-strain (transverse strain ε_x and vertical strain ε_y) responses of the material under in-plane tension load. It can be seen from Fig. 15 that the vertical stress-strain response exhibits linear characteristic, while the transverse response shows a non-linear characteristic with the applied load increase. The failure strain is around 0.7% in both warp and weft direction tension experiments. However, the elastic modulus (14.3 GPa) and tensile strength (100 MPa) in warp direction are much higher than those in weft direction (elastic modulus: 7.6 GPa; tensile strength: 50 MPa). The volume fractions of warp and weft yarns are 30.13% and 12.85% respectively. So we could infer that the warp yarn has lower mechanical properties in the loading direction due to the crimp characteristic. However, the warp yarn enhances the mechanical properties in out-of-plane direction, and has a significant influence on the strain/stress distribution inside the material, which

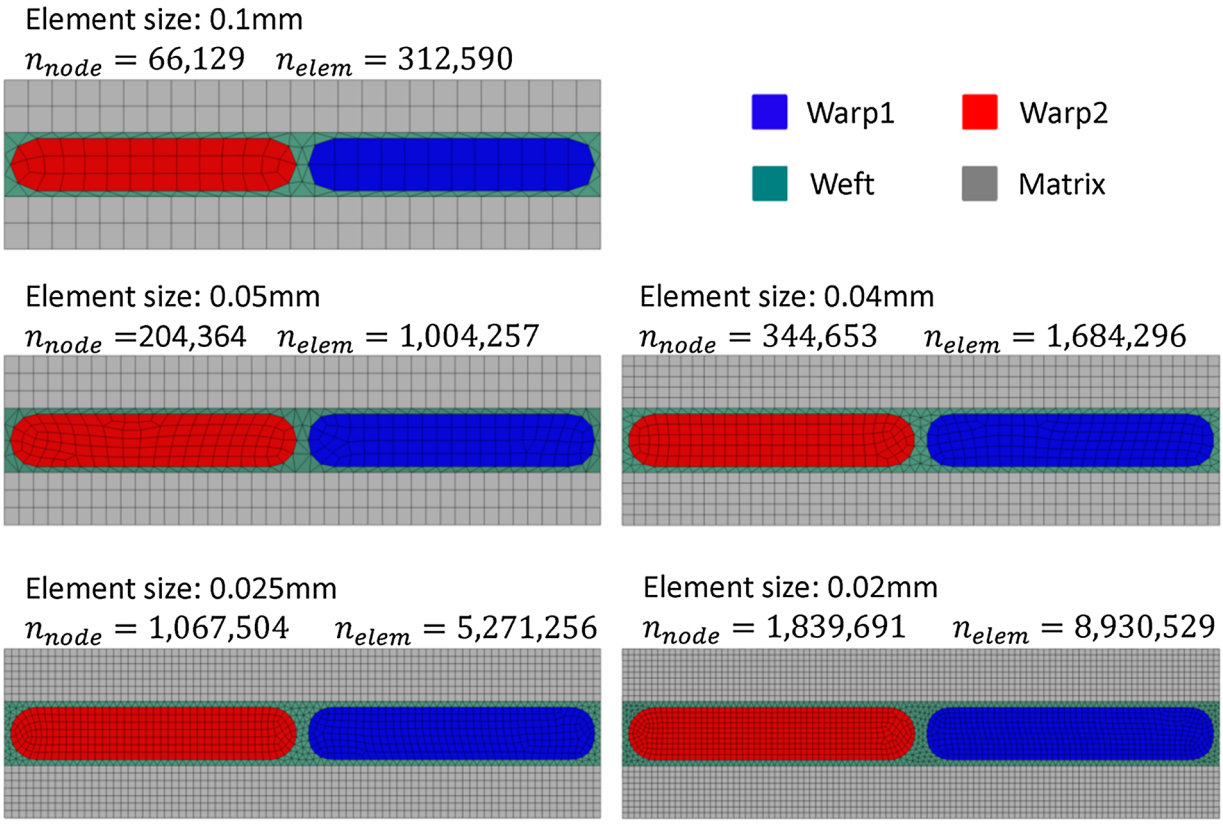

Fig. 10. Meshed models with different element size.

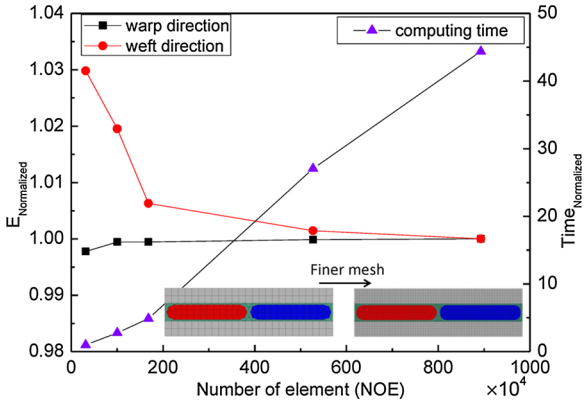

Fig. 11. Normalized moduli and computing time as a function of element number.

would be described later.

The transverse stress-strain responses exhibit non-linear behavior and differ a lot under warp/weft direction loadings, see Fig. 15. The crimp deformation of yarns is the major reason for the transverse responses nonlinearity. Under warp direction tensile loading, the weft yarn in transverse direction becomes curved from straight, resulting in a larger negative strain and the nonlinearity. While under weft direction tensile loading, the weft yarn in loading direction is straight, and the strain in weft yarn has little influence on the curviness of warp yarn in transverse direction, thus the transverse strain is much lower. The transverse response nonlinearity causes the Poisson's ratio of the material to be not a constant during the loading process. The Poisson' ratio exhibits an increasing tendency with the applied tensile stress increase, which varies from 0.05 ~ 0.2 and 0.03 ~ 0.14 under warp/weft direction tensile loading, respectively.

4.1.3. Strain extracted with different methods

Fig. 16 shows the vertical strain extracted by DIC method and strain gauge, respectively. The size of the strain gauge is 2 mm × 4 mm. In the case of warp direction loading, the strain gauge covers about a half of unit cell surface. However, the strain gauge has a strain value of approximately 90% of the value calculated by DIC method. Due to the sol-gel method, the matrix filling of the specimen surface is insufficient, and the fiber bundle protrudes from the specimen surface. Therefore, the strain gauge is only attached to the fiber bundles. According to the analysis earlier, the matrix has a larger strain than fiber bundle on the specimen surface. Besides, the size and position of the strain gauge have a significant influence on the measured result (The strain distribution on the unit cell surface fluctuates with the strain gauge size and position, this will be elaborated in section 4.2.2). Hence the strain value measured by the strain gauge has some deviation compared with actual average strain. The DIC method could capture the displacement information of both fiber bundles and matrix, and cover the entire surface of the specimen. Therefore, the strain extracted by DIC method is closer to actual average strain.

In the case of weft direction loading, the vertical strain exhibits a linear behavior with the load increase. However, the strain value extracted by strain gauge is about 84% of the value calculated by DIC technique. One reason is that, the size of strain gauge is not large enough to cover sufficient area of specimen surface. The width of strain gauge is 2 mm while the length of unit cell in warp direction is 6.82 mm, so the measured strain has a large deviation (discussed in section 4.2.2). Besides, as mentioned earlier, the matrix filling of the specimen surface is insufficient, thus the strain gauge is only attached to the fiber bundles. Therefore, when measuring the strain of woven composites, DIC method is recommended as the top priority due to its accuracy and full-field measurement capability.

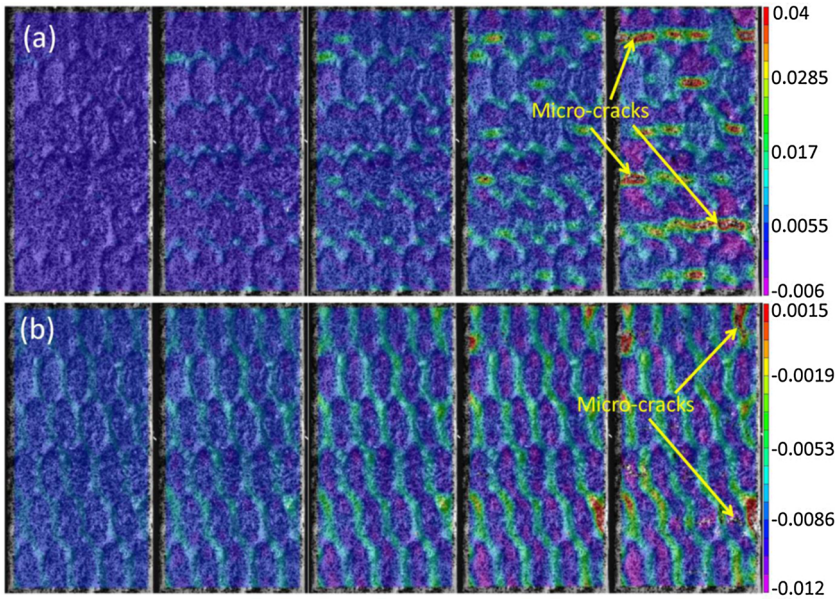

Fig. 12. Evolutions of full-field strains at warp direction tensile stress of 20 MPa, 40 MPa, 60 MPa, 80 MPa and 100 MPa: (a) vertical strain; (b) transverse strain.

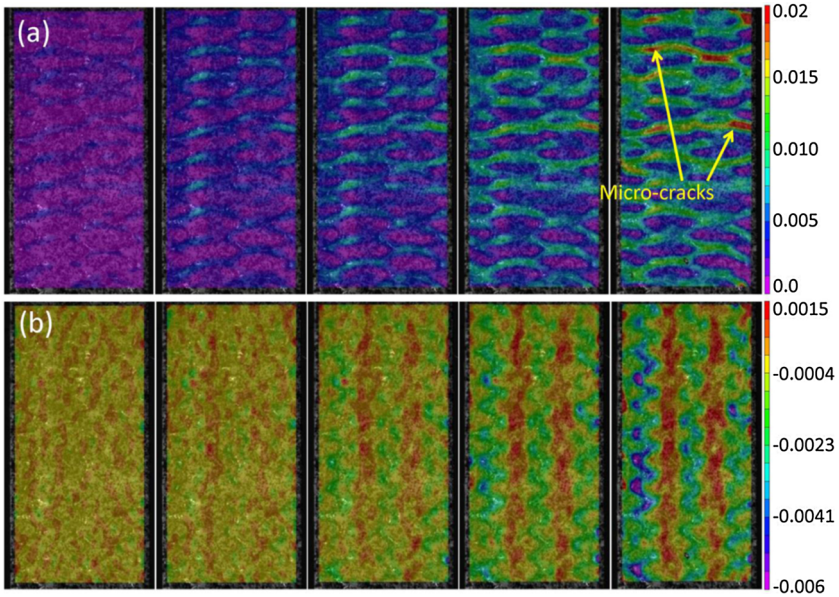

Fig. 13. Evolutions of full-field strains at weft direction tensile stress of 10 MPa, 20 MPa, 30 MPa, 40 MPa and 50 MPa: (a) vertical strain; (b) transverse strain.

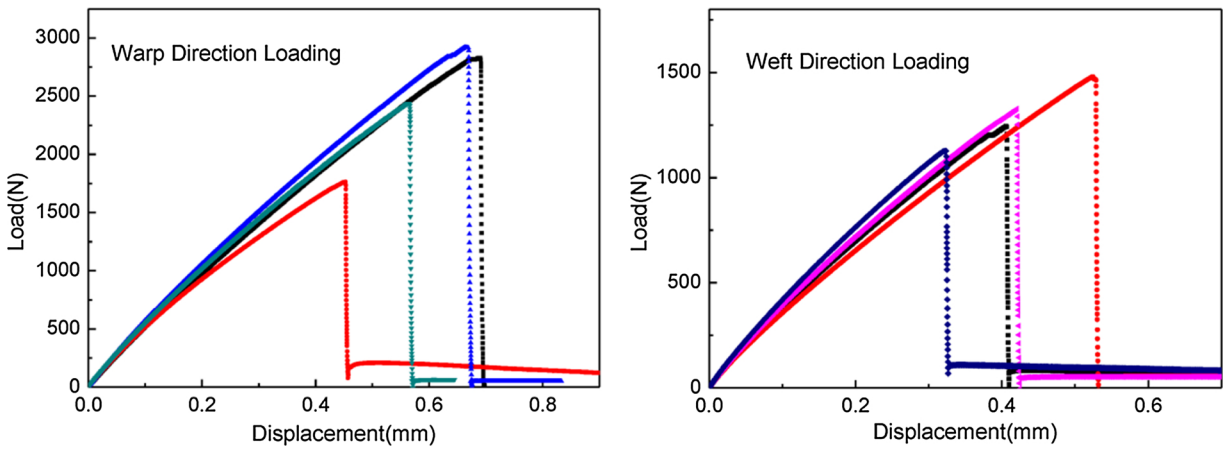

Fig. 14. In-plane tension load-displacement responses of the 2.5D woven SiO_{2f}/SiO_2 composite (warp/weft direction).

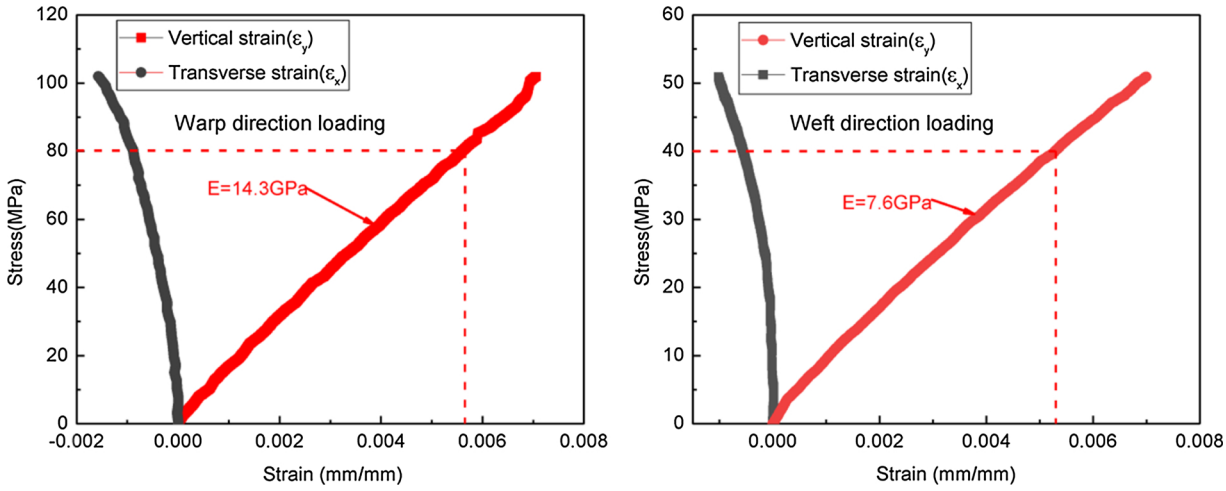

Fig. 15. In-plane tension stress-strain curve of the 2.5D woven SiO_{2f}/SiO_2 composite (warp/weft direction).

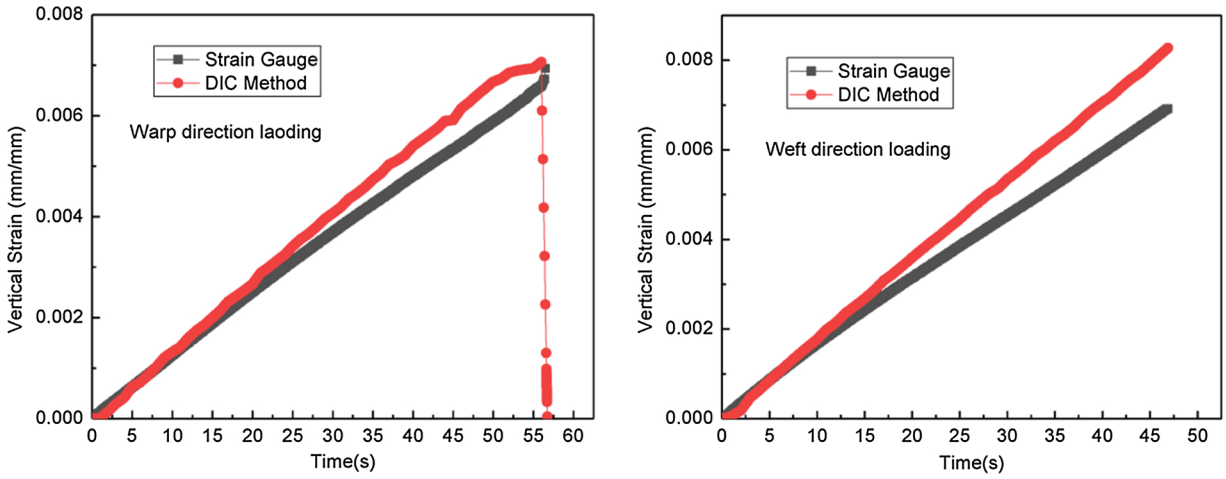

Fig. 16. Vertical strain extracted by DIC method and strain gauge.

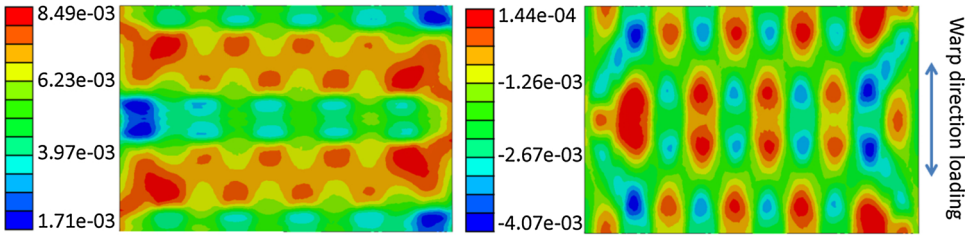

Fig. 17. Surface strain distributions upon warp direction tensile loading (vertical/transverse strain, unit: mm/mm).

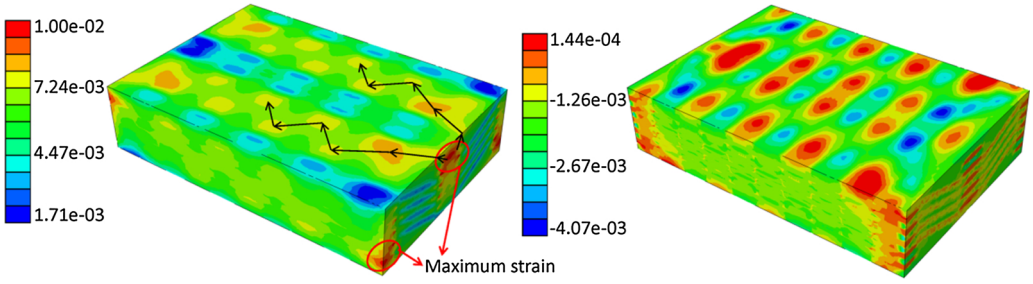

Fig. 18. Strain distributions upon warp direction tensile loading (vertical/transverse strain, unit: mm/mm).

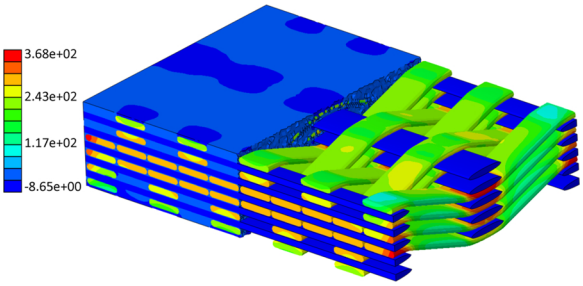

Fig. 19. Vertical stress distribution upon warp direction tensile loading (MPa).

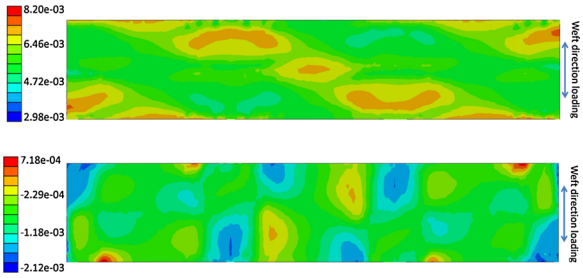

Fig. 20. Surface strain distributions upon weft direction tensile loading (vertical/transverse strain, unit: mm/mm).

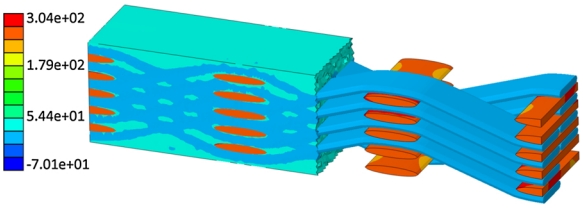

Fig. 21. Vertical stress distribution upon weft direction tensile loading (MPa).

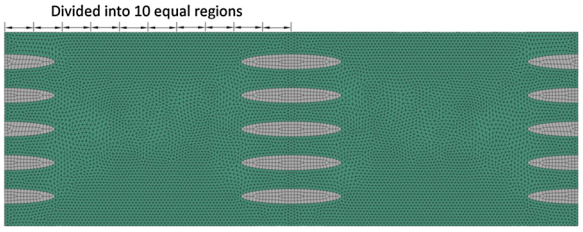

Fig. 22. Schematic of region division of the unit cell surface in warp direction.

4.2. Numerical investigation

4.2.1. Stress/strain distribution

Fig. 17 shows the vertical and transverse strain distributions of the 2.5D woven composite with a 0.6% tensile strain in warp direction. The strain of the matrix is obviously affected by the crimp of the fiber yarns. In the green region on the surface, the strain is small due to the thin thickness of matrix, and the fiber yarns are adjacent to the surface. While in the matrix-rich region, the fiber yarns extend downward, resulting in large strain on the matrix surface. The vertical strain shows a zig-zag shape that connects the matrix-rich regions to each other, which is consistent with the strain distribution measured by DIC method in Fig. 12, and the micro-cracks initiate and propagate along the zig-zag path.

Fig. 18 shows the vertical and transverse strain distribution of the established model. The strain values vary greatly in different regions. The maximum strain occurs in the region between the two weft yarns, between which there is no warp yarn passing through. This is the result of the combined action of tension loading in X direction and warp squeezing in Y direction. Matrix cracks are more likely to initiate in this region and propagate to the surface of the specimen, and cause cracks on the specimen surface. The possible crack propagation paths are shown by the black arrows in Fig. 18.

The vertical stress distribution of the fiber bundles and matrix is shown in Fig. 19. It can be seen that, the warp yarns carry the external load while the weft yarns do not carry at all. This is because the external load transfers to warp yarns directly, after which the load transfers to matrix and then the weft yarns. Due to the weak load carrying capacity of the matrix, the load transmitted to the weft yarns is also small. The maximum vertical stress of warp yarns occurs at the arc area where the warp yarn and weft yarn squeeze each other. For a single warp yarn, the maximum stress appears on the inner side of the arc area, where the warp yarn presses on the adjacent weft yarn. With the uniaxial tension in warp direction, the warp yarns have a tendency to straighten (curvature reduction), and the arc area produces an inward displacement and presses on the adjacent weft yarn. The strain in this region is also the maximum as illustrated above; therefore it is the most dangerous area and should be considered during design and use. The transverse stress is approximately one tenth of the vertical stress, and would not cause major damage to the material.

The uniaxial tension in weft direction is simulated with a tensile strain of 0.6% on the FE model. The surface strain distributions in both vertical direction and transverse direction are shown in Fig. 20. The periodic and non-uniform stress/strain distribution can be observed, which attribute to the weave architecture of the composite. And similar to the warp direction loading, the matrix adjacent to the yarns has a larger strain; and the weft yarns carry the external load while the vertical stress of matrix and warp yarns are much smaller (see Fig. 21).

4.2.2. Volatility of surface strain distribution

The vertical strain in different regions is calculated to have an in-depth understanding of the strain distribution on the woven composite surface. The unit cell surface is divided into twenty equal regions in the warp direction (Fig. 22), and the average strain of each region is calculated by extracting the strain values on the nodes attached to the region and averaging these values. The average strain of each region is plotted in Fig. 23(a). The vertical coordinate represents the vertical strain of each region, and the horizontal coordinate indicates the center position of each region. It can be seen from Fig. 23(a) that, the strain is symmetrically distributed about the center of the unit cell, since the weave architecture is antisymmetric. According to the finite element method (FEM) simulation, the strain in the area near the fiber bundle (X = 0 ~ 0.1, 0.9 ~ 1) is 13% lower than the average value, and in the matrix-rich region (X = 0.4 ~ 0.5), the strain is 15% larger than the average value. The vertical strains in different regions are also extracted with DIC method (red line in Fig. 23(a), Fig. 23(b)). The strain distribution shows the same fluctuation characteristic as the simulation result. The vertical strains in region 4, 5 and 6 are higher than the average strain. But the maximum fluctuation reaches 30%, this is caused by the deviation between the real specimen and the ideal FE model.

Fig. 24 shows the average strain in accumulated regions. Although the maximum strain deviation in a unit cell reaches 30% (DIC result), the average strain approaches the average value with the increase of accumulated regions. When the accumulated regions exceed 1/2 unit cell surface, the maximum deviation is 4.3% (DIC result); when exceed one unit cell surface, the maximum deviation is 2.3% (DIC result). Therefore, when extracting the strain by strain gauge or DIC method, the concerned area should contain at least one unit cell to eliminate the

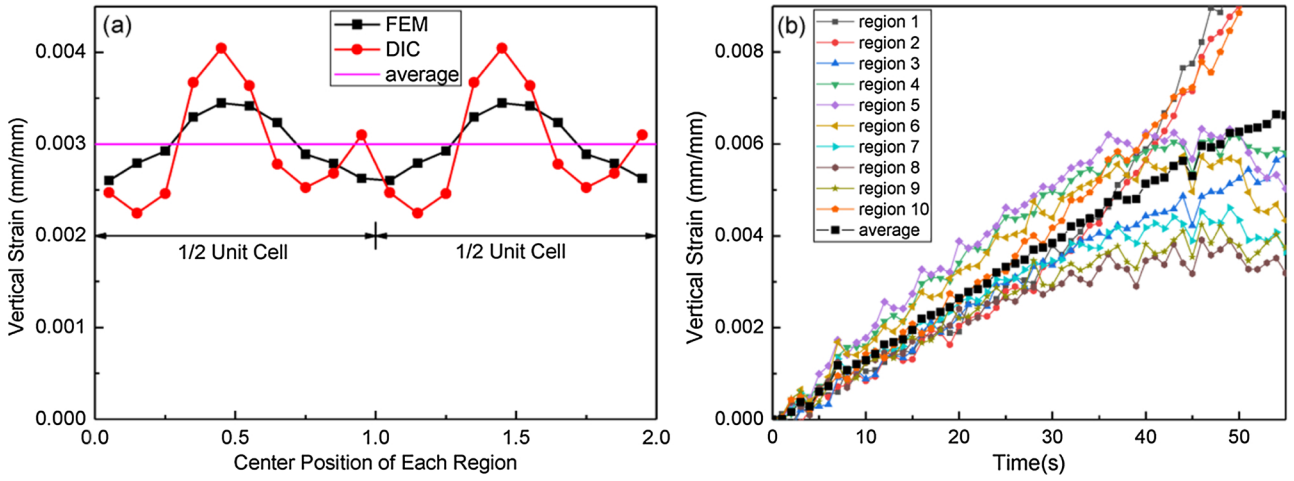

Fig. 23. Vertical strain (strain in warp direction) distribution in different regions: (a) Comparison between FEM simulation and DIC result at an average vertical strain of 0.003; (b) Vertical strain evolution process in different regions during the test, extracted with DIC method.

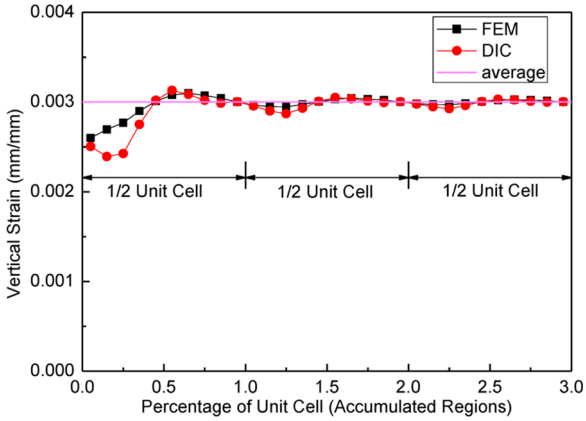

Fig. 24. Average vertical strain (strain in warp direction) in accumulated regions.

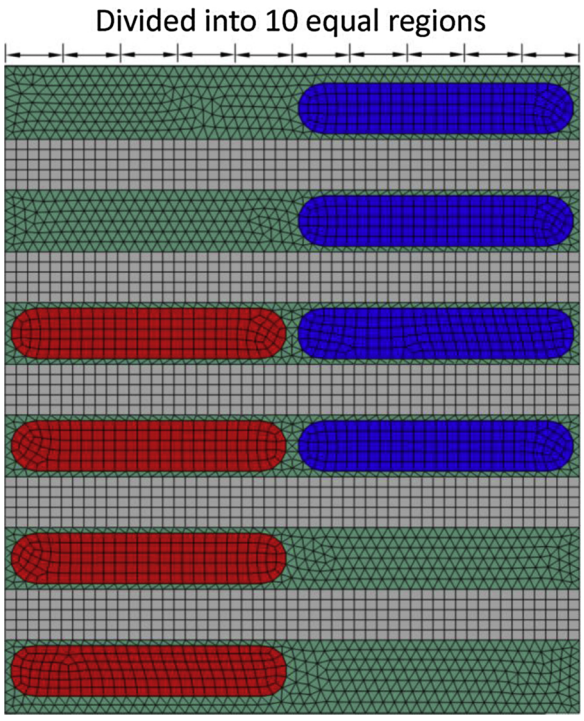

Fig. 25. Schematic of region division of the unit cell surface in weft direction.

effects of non-uniform distribution. And if the fluctuation of strain distribution gets larger, more unit cell regions should be covered to obtain accurate results.

In the weft direction, the surface of unit cell is divided into ten equal regions as shown in Fig. 25. The average strain of each region is plotted in Fig. 26(a). The vertical coordinate represents the average vertical strain (weft direction) of each region, and the horizontal coordinate represents the center position of each region. The strain fluctuates in a unit cell region due to the weave architecture of yarns. According to the DIC result (red line in Fig. 26(a)), the maximum strain is 30% larger than the average value, and the minimum strain is 21% lower than the average. However, the strain fluctuation of FEM simulation is much lower than experiment. Fig. 26(b) shows the vertical strain of each region extracted by DIC method. The vertical strains in region 2, 3 and 4 are higher than the average strain, which matches the simulation results (Fig. 26 (a)). And the maximum fluctuation is about 30%.

The difference between the simulation results and test results is mainly caused by the difference between the established FE model and the test specimen. On the one hand, during the manufacture process of the specimen, the fiber tows were squeezed in the thickness direction and then deformed, especially the fiber tows on the surface of specimen (orange area in Fig. 27). However, this deformation is not constructed in the FE model; on the other hand, due to the weave architecture of the fiber tows, the specimen surface is uneven (see Fig. 27). The regions between the adjacent fiber tows are not completely filled with the matrix, which influences the load transfer between the fiber tows, especially for the load transfer between the warp tows during the weft direction loading (blue area in Fig. 27). Therefore, the strain non-uniformity in test results is much more significant than that in simulation results.

Fig. 28 shows the average strain in accumulated regions. Similar to the result in warp direction, the average strain approaches the average value with the increase of the accumulated regions. When the accumulated regions exceed one unit cell surface, the maximum deviation is 3.5% (DIC result); when exceed two unit cell surfaces, the maximum deviation is 1.8% (DIC result).

According to the above analysis, the fluctuation of the surface

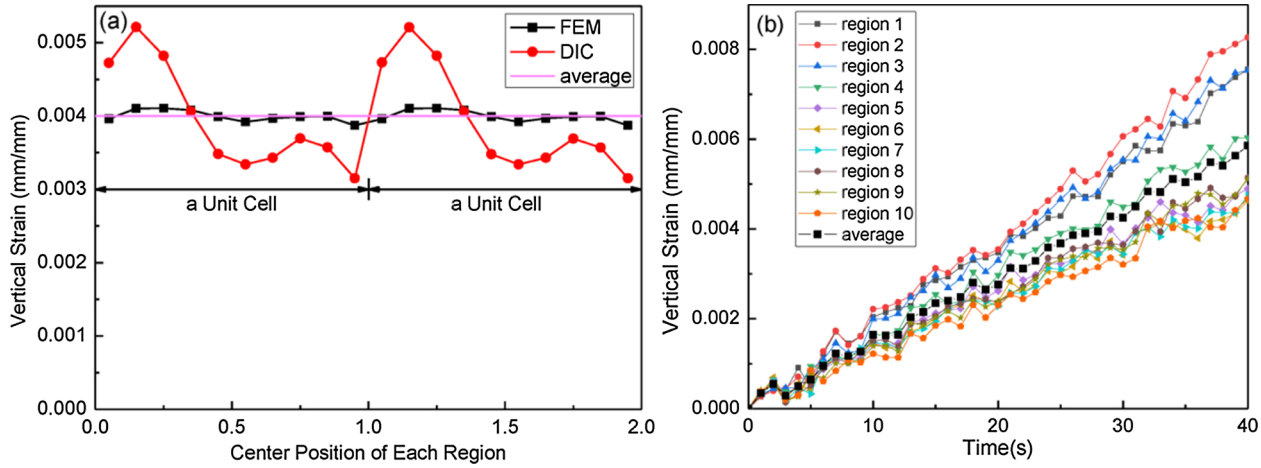

Fig. 26. Vertical strain (strain in weft direction) distribution in different regions: (a) Comparison between FEM simulation and DIC result at an average vertical strain of 0.004; (b) Vertical strain evolution process in different regions during the test process, extracted with DIC method.

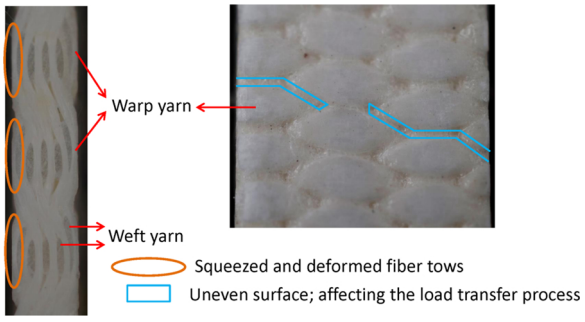

Fig. 27. Enlarged local diagram of the 2.5D woven composite.

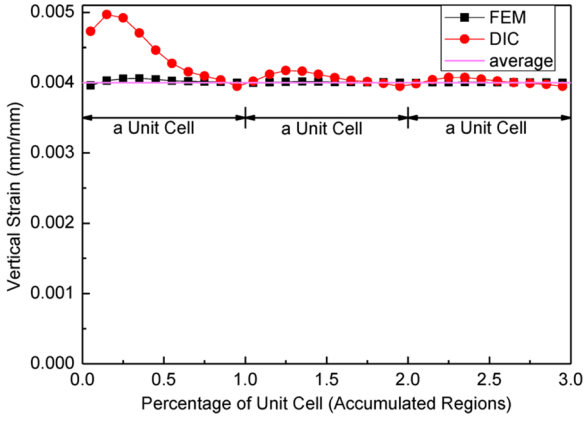

Fig. 28. Average vertical strain (strain in weft direction) in accumulated regions.

strains are large (about 30%) in the experiments. Therefore, a larger calculation region should be covered to obtain the accurate average strain. To achieve this, the size of strain gauge should be greater than twice the size of unit cell, and it would be better if the size of the strain gauge is an integer multiple of the unit cell size in both warp and weft directions. The same requirements should also be met when the strain is extracted by the DIC method.

4.2.3. *Effect of local coordinate system*

The simulations of the model without considering local coordinate systems were analyzed to study its effect on the vertical strain distribution, as shown in Fig. 29. The vertical strain distributions have the similar characteristics as those in section 4.2.1, but the distributions are more even, especially in warp direction loading. This indicates that the simulation results without considering the local coordinate systems are less conservative and may cause serious damage to the material or structure. Therefore, accurate local coordinate systems are essential and necessary to obtain accurate results in design and analysis process.

5. Conclusions

In this paper, the in-plane on-axis tensile tests of a 2.5D fiber-reinforced woven SiO_{2f}/SiO_2 composite including warp and weft directions were conducted. Full-field deformation/strain distributions of the specimen surfaces were obtained with DIC technique. The established finite element models of the material contain the full thickness of the material to simulate the strain distribution accurately. Besides, local coordinate systems were assigned on each node of warp yarns by rotating the global coordinate system, which simplifies the modeling process as well as improves the accuracy of numerical simulation. According to the experimental and numerical simulation results, some valuable conclusions can be drawn as follows:

(1) The strain distributions of the 2.5D woven composite are related with the weave architecture. The strain on the surface of the specimen has a periodic distribution due to the weave architecture of fiber yarns.

(2) Upon on-axis loading conditions, the external load is carried by the yarns along the loading direction, while the transverse yarns carry much less load. This is due to that the stress of transverse yarns is transferred by matrix, and the load capacity of matrix is much lower compared with fiber yarns.

(3) The maximum strain fluctuation of the specimen surface is about 30% during the experiment process. With the calculated area increase, the average strain deviation decreases rapidly.

(4) To obtain the accurate average strain of woven composite, the size of strain gauge should be twice larger than the size of unit cell, and much more accurate result could be obtained if the size of the strain gauge is an integer multiple of the unit cell size in both warp and weft directions. Same requirements should also be met when the strain is extracted with DIC method.

(5) The local coordinate systems of warp yarns have an obvious influence on the stress/strain distribution, especially in warp direction loading. Assigning local coordinate systems are essential and necessary to guarantee the accuracy and reliability of simulation results.

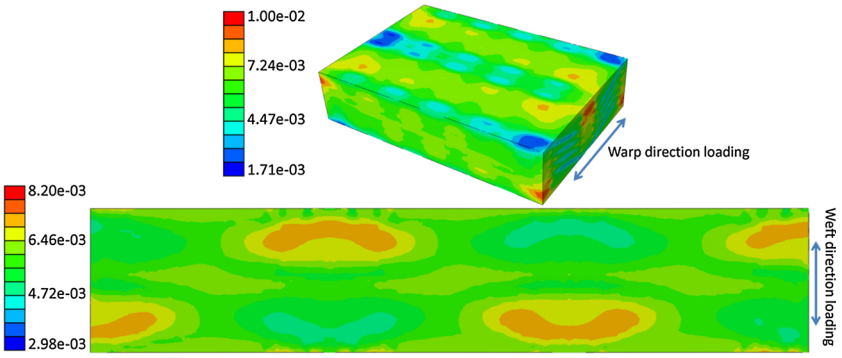

Fig. 29. Vertical strain (unit: mm/mm) distributions without considering local coordinate systems: (a) Warp direction loading; (b) Weft direction loading.

Acknowledgement

This work was supported by the National Natural Science Foundation of China [Grant No. 51772009, 51802264 and 51275023].

References

[1] AIAA, Ceramic matrix composites to make breakthroughs in aircraft engine performance[C]// Aiaa/asme/asce/ahs/asc structures, Struct. Dyn. Mater. Conf. (2009), https://doi.org/10.2514/6.2009-2675.
[2] Y. Katoh, L.L. Snead, C.H.H. Jr, et al., Current status and recent research achievements in SiC/SiC composites, J. Nucl. Mater. 455 (1–3) (2014) 387–397, https://doi.org/10.1016/j.jnucmat.2014.06.003.
[3] Q. Liu, J. Paavola, Lightweight design of composite laminated structures with frequency constraint, Compos. Struct. 156 (2016) 356–360, https://doi.org/10.1016/j.compstruct.2015.08.116.
[4] J. Li, G. Jiao, B. Wang, Designable in-plane mechanical property of plain-woven C/SiC composite laminate, J. Mech. Strength 34 (2) (2012) 229–233, https://doi.org/10.16579/j.issn.1001.9669.2012.02.010.
[5] A. Hallal, R. Younes, F. Fardoun, et al., Improved analytical model to predict the effective elastic properties of 2.5D interlock woven fabrics composite, Compos. Struct. 94 (10) (2012) 3009–3028, https://doi.org/10.1016/j.compstruct.2012.03.019.
[6] C. Zhang, M. Zhao, Y. Liu, et al., Tensile strength degradation of a 2.5D-C/SiC composite under thermal cycles in air, J. Eur. Ceram. Soc. 36 (12) (2016) 3011–3019, https://doi.org/10.1016/j.jeurceramsoc.2015.12.007.
[7] Y. Liu, J. Zhu, Z. Chen, et al., Mechanical properties and microstructure of 2.5D (shallow straight-joint) quartz fibers-reinforced silica composites by silicasol-in-filtration-sintering, Ceram. Int. 38 (1) (2012) 795–800, https://doi.org/10.1016/j.ceramint.2011.08.006.
[8] Z. Lu, Y. Zhou, Z. Yang, et al., Multi-scale finite element analysis of 2.5D woven fabric composites under on-axis and off-axis tension, Comput. Mater. Sci. 79 (2013) 485–494, https://doi.org/10.1016/j.commatsci.2013.07.003.
[9] J. Song, W. Wen, H. Cui, Experimental and numerical investigation of mechanical behaviors of 2.5D woven composites at ambient and un-ambient temperatures, Compos. Struct. (2018), https://doi.org/10.1016/j.compstruct.2018.06.054.
[10] B. Sun, B. Gu, X. Ding, Compressive behavior of 3-D angle-interlock woven fabric composites at various strain rates, Polym. Test. 24 (4) (2005) 447–454, https://doi.org/10.1016/j.polymertesting.2005.01.005.
[11] L. Yu, B. Pan, Experimental Study of tensile properties and deformation evolutions of 2D and 2.5D woven SiO_{2f}/SiO_2 composites using single-camera stereo-digital image correlation, Compos. Struct. (2018), https://doi.org/10.1016/j.compstruct.2018.05.135.
[12] L. Qin, Z. Zhang, X. Li, et al., Full-field analysis of shear test on 3D orthogonal woven C/C composites, Compos. Part A Appl. Sci. Manuf. 43 (2) (2012) 0–316, https://doi.org/10.1016/j.compositesa.2011.11.006.
[13] M.N. Rossol, V.P. Rajan, F.W. Zok, Effects of weave architecture on mechanical response of 2D ceramic composites, Compos. Part A Appl. Sci. Manuf. 74 (2015) 141–152, https://doi.org/10.1016/j.compositesa.2015.04.003.
[14] V.P. Rajan, M.N. Rossol, F.W. Zok, Optimization of digital image correlation for high-resolution strain mapping of ceramic composites, Exp. Mech. 52 (9) (2012) 1407–1421, https://doi.org/10.1007/s11340-012-9617-1.
[15] D. Ivanov, S. Ivanov, S. Lomov, et al., Strain mapping analysis of textile composites, Opt. Lasers Eng. 47 (3–4) (2009) 360–370, https://doi.org/10.1016/j.optlaseng.2008.05.013.
[16] S. Dai, P.R. Cunningham, S. Marshall, et al., Influence of fibre architecture on the tensile, compressive and flexural behaviour of 3D woven composites, Compos. Part A Appl. Sci. Manuf. 69 (2015) 195–207, https://doi.org/10.1016/j.compositesa.2014.11.012.
[17] E. Archer, J. Broderick, A.T. Mcilhagger, Internal strain measurement and cure monitoring of 3D angle interlock woven carbon fibre composites, Compos. Part B Eng. 56 (12) (2014) 424–430, https://doi.org/10.1016/j.compositesb.2013.08.067.
[18] V. Mazars, O. Caty, G. Couégnat, et al., Damage investigation and modeling of 3D woven ceramic matrix composites from X-ray tomography in-situ tensile tests, Acta Mater. (2017) 140, https://doi.org/10.1016/j.actamat.2017.08.034.
[19] L. Saucedo-Mora, T. Lowe, S. Zhao, et al., In situ observation of mechanical damage within a SiC-SiC ceramic matrix composite, J. Nucl. Mater. 481 (2016) 13–23, https://doi.org/10.1016/j.jnucmat.2016.09.007.
[20] B. Rahmani, E. Ghossein, I. Villemure, et al., In-situ mechanical properties identification of 3D particulate composites using the Virtual Fields Method, Int. J. Solids Struct. 51 (18) (2014) 3076–3086, https://doi.org/10.1016/j.ijsolstr.2014.05.006.
[21] B.K. Bay, T.S. Smith, D.P. Fyhrie, et al., Digital volume correlation: three-dimensional strain mapping using X-ray tomography, Exp. Mech. 39 (3) (1999) 217–226, https://doi.org/10.1007/bf02323555.
[22] S.V. Lomov, D.S. Ivanov, I. Verpoest, et al., Full-field strain measurements for validation of meso-FE analysis of textile composites, Compos. Part A Appl. Sci. Manuf. 39 (8) (2008) 0–1231, https://doi.org/10.1016/j.compositesa.2007.09.011.
[23] J.H. Shaw, V.P. Rajan, M. Blacklock, et al., Towards virtual testing of textile composites: calibration of thermoelastic tow properties, J. Am. Ceram. Soc. 97 (4) (2014) 1209–1217, https://doi.org/10.1111/jace.12829.
[24] M. Blacklock, J.H. Shaw, F.W. Zok, et al., Virtual specimens for analyzing strain distributions in textile ceramic composites, Compos. Part A Appl. Sci. Manuf. 85 (2016) 40–51, https://doi.org/10.1016/j.compositesa.2016.02.030.
[25] G. Nicoletto, G. Anzelotti, E. Riva, Mesoscopic strain fields in woven composites: experiments vs. Finite element modeling, Opt. Lasers Eng. 47 (3–4) (2009) 352–359, https://doi.org/10.1016/j.optlaseng.2008.07.009.
[26] L.I. Bin, L.I. Duan, C. Zhang, et al., Preparation and properties of SiO_(2f)/SiO_2-BN composites, Acta Materiae Compositae Sinica 21 (3) (2011) s374–s379, https://doi.org/10.13801/j.cnki.fhclxb.2011.03.024.
[27] H.L. Liu, Strength Analysis of 2.5 Dimensional Woven Fan Stator Vane/Casing Connectional Structure [Master Thesis], Nanjing University of Aeronautics and Astronautics, 2014.
[28] Z. Lu, Z. Yuan, Q. Liu, 3D numerical simulation for the elastic properties of random fiber composites with a wide range of fiber aspect ratios, Comput. Mater. Sci. 90 (2014) 123–129, https://doi.org/10.1016/j.commatsci.2014.04.007.
[29] T. Gao, Y. Zhao, G. Zhou, et al., Fabrication and characterization of three dimensional woven carbon fiber/silica ceramic matrix composites, Compos. Part B Eng. 77 (2015) 122–128, https://doi.org/10.1016/j.compositesb.2015.02.024.
[30] Y. Liu, Influence of Quartz Fabric Structures on the Mechanical Properties of Silica Matrix Composites [PhD Thesis], Nanjing University of Aeronautics and Astronautics, 2013.